

# Understanding variations in downwelling longwave radiation using Brutsaert's equation

Yinglin Tian<sup>1,2</sup>, Deyu Zhong<sup>1</sup>, Sarosh Alam Ghausi<sup>2,3</sup>, Guangqian Wang<sup>1</sup>, Axel Kleidon<sup>2</sup>

<sup>1</sup>State Key Laboratory of Hydrosience and Engineering, Department of Hydraulic Engineering, Tsinghua University, 100084 Beijing, China.

<sup>2</sup>Biospheric Theory and Modelling, Max Planck Institute for Biogeochemistry, 07701 Jena, Germany

<sup>3</sup>International Max Planck Research School on Global Biogeochemical Cycles (IMPRS-gBGC), 07701 Jena, Germany

Correspondence to: Axel Kleidon ([akleidon@bgc-jena.mpg.de](mailto:akleidon@bgc-jena.mpg.de))

## Abstract

A dominant term in the surface energy balance and central to global warming is downwelling longwave radiation ( $R_{ld}$ ). It is influenced by radiative properties of the atmospheric column, in particular by greenhouse gases, water vapour, clouds and differences in atmospheric heat storage. We use the semi-empirical equation derived by Brutsaert (1975) to identify the leading terms responsible for the ~~spatio-temporal~~ spatial-temporal climatological variations in  $R_{ld}$ . This equation requires only near-surface observations of air temperature and humidity. We first evaluated this equation and its extension by Crawford and Duchon (1999) with observations from FLUXNET, the NASA-CERES dataset, and the ERA5 reanalysis. We found a strong ~~temporal~~ spatiotemporal ~~spatial~~ correlation between estimated  $R_{ld}$  and the datasets above, with  $r^2$  ranging from ~~0.87 to 0.98~~ 0.87 to 0.98 across the datasets for clear-sky and all-sky conditions. ~~We then used the equations to show that changes in atmospheric heat storage explain more than 95% of diurnal range in  $R_{ld}$ . Moreover, around 73% of  $R_{ld}$  seasonal variations are led by atmospheric heat storage on a global scale, with the regional contribution increasing with latitude. Seasonal changes in the emissivity of the atmosphere play a second role, which is controlled by anomalies in cloud cover at high latitudes but dominated by water vapor changes at mid-latitude and subtropics, especially over monsoon regions. We also found that as aridity increases over region, the contributions from changes in emissivity and atmospheric heat storage tend to offset each other ( $-40 \text{ W m}^{-2}$  and  $20-30 \text{ W m}^{-2}$ , respectively), explaining the relatively small decrease in  $R_{ld}$  with aridity ( $-(10-20) \text{ W/m}^{-2}$ ).~~ We then used the equations to show that changes in lower-level atmospheric heat storage explain more than 95% and around 73% of diurnal range and seasonal variations in  $R_{ld}$ , respectively, with the regional contribution decreasing with latitude. Seasonal changes in the emissivity of the atmosphere play a second role, which is controlled by anomalies in cloud cover at high latitudes but dominated by water vapor changes at mid-latitude and subtropics, especially over monsoon regions. We also found that as aridity increases over region, the contributions from changes in emissivity and lower-level atmospheric heat storage tend to offset each other ( $-40 \text{ W m}^{-2}$  and  $20-30 \text{ W m}^{-2}$ , respectively), explaining the relatively small decrease in  $R_{ld}$  with aridity ( $-(10-20) \text{ W/m}^{-2}$ ). These equations thus provide a solid physical basis for understanding the spatiotemporal variability of surface downwelling longwave radiation. This should help to better understand and interpret climatological changes, such as those associated with extreme events and global warming.

## 42 1 Introduction

43 In the global mean surface energy budget, downward longwave radiation ( $R_{ld}$ ) is ~~dominant surface energy~~  
44 ~~input~~ ~~the dominant energy input to surface~~ (333 W/m<sup>2</sup> ~~in global mean and 306 W<sup>2</sup>/m over land~~), contributing  
45 ~~more than around~~ twice as much energy as absorbed solar radiation (161 W/m<sup>2</sup> ~~in global mean and 184~~  
46 ~~W<sup>2</sup>/m over land~~) (Trenberth et al. 2009, Wild et al. 2015). This dominance holds over all regions in the  
47 climatological mean, although there are some clear variations in space and time (Figs. ~~ure~~ 1 and S1). It is  
48 central to global warming, reflecting the greenhouse effect of the atmosphere (Held and Soden 2000), and  
49 its variations have been suggested to be the main contributor to some regional warming amplifications, such  
50 as in the Arctic (Lee et al. 2017) and the Tibetan Plateau (Su et al. 2017). Therefore, it is important to  
51 understand the main sources of variations in this surface energy balance term, which can be seen in Figure  
52 1.

53 The flux of downwelling longwave radiation is influenced by the radiative properties of the entire  
54 atmospheric column, i.e., water vapour, clouds, and greenhouse gases, but also by the heat stored in the  
55 atmosphere, i.e., the temperature at which radiation is emitted back to the surface. To obtain an estimate of  
56 this flux, Brutsaert (1975) used functional expressions for the typical temperature and humidity profiles of  
57 the lower troposphere together with radiative transfer equations and semiempirical relationships of the  
58 absorptivity by water vapor, integrated these vertically, and expressed the resulting flux  $R_{ld}$  in terms of near-  
59 surface air temperature and water vapour pressure for clear-sky conditions. He thereby derived a semi-  
60 empirical equation for  $R_{ld}$  for an effective clear sky emissivity ( $\epsilon_{cs}$ ) and the corresponding flux of  
61 downwelling longwave radiation ( $R_{ld,cs}$ ):

$$\epsilon_{cs} = 1.24(e_a/T_a)^{1/7}, \quad (1)$$

$$R_{ld,cs} = \epsilon_{cs}\sigma T_a^4. \quad (2)$$

62 where  $\sigma$  is Stefan–Boltzmann constant ( $\sigma = 5.67 \cdot 10^{-8} \text{ W m}^{-2} \text{ K}^{-4}$ ),  $e_a$  is the 2m water vapor pressure (unit:  
63 millibars) and  $T_a$  is the 2m air temperature (unit: K). The latter two meteorological variables can easily be  
64 obtained or inferred from weather stations, so that the downwelling flux of longwave radiation can be  
65 estimated from weather station observations. Note that the  $\epsilon_{cs}$  shown in equation 1 is largely insensitive to  
66 changes in  $T_a$ . As a result, emissivity does not have a direct dependence on  $T_a$ , except that higher  
67 temperature may also lead to higher values in  $e_a$ .

69 This equation was later extended to all-sky conditions that include the effects of cloud cover, among which  
70 Crawford and Duchon (1999) is a common extension (Alados et al. 2012; Duarte et al. 2006; Flerchinger  
71 et al. 2009). This extension diagnoses cloud cover fraction ( $f_c$ ) as the fraction of incoming solar radiation  
72 at the surface ( $R_s$ ) in relation to the potential solar radiation ( $R_{s,pot}$ ), that is, the incoming flux at the top of  
73 the atmosphere. The emissivity for all-sky conditions,  $\epsilon$ , is then calculated as the mix of the emissivities of  
74 clear-sky conditions (Eqn. (1), weighted by the cloud-free proportion,  $(1 - f_c)$ ) and clouds with an  
75 emissivity of  $\epsilon_c = 1$  (weighted by the cloud fraction  $f_c$ ). Using this emissivity, the estimation of  
76 downwelling longwave radiation is then done by

$$f_c = 1 - R_s/R_{s,pot}, \quad (3)$$

$$\epsilon = f_c + (1 - f_c)\epsilon_{cs}, \quad (4)$$

$$R_{ld} = \epsilon\sigma T_a^4. \quad (5)$$

77 Previous studies have already verified Equations 4-5 to have a very good agreement with site measurements  
78 ~~with the R<sup>2</sup> of 0.883 and RMSE of 15.367 W/m<sup>2</sup> with the rR<sup>2</sup> of 0.883 and RMSE of 15.367 W/m<sup>2</sup>~~ (Duarte et al.  
79 2006; Hatfield et al. 1983), especially when the temperature is higher than 0°C (Aase and Idso 1978;

设置了格式: 上标

批注 [SG1]: This sentence is unclear. I have suggested an alternative.

设置了格式: 英语(英国)

设置了格式: 字体: (中文)+中文正文(宋体), (中文) 简体中文(中国大陆)

格式化表格

80 Satterlund 1979). Other studies have worked to calibrate and modify this estimate further to different  
81 regions (Malek 1997; Sridhar and Elliott 2002).

82 This expression for downwelling longwave radiation  $R_{ld}$  given by Eqn. (5) allows us to quantify the different  
83 contributions by cloud cover,  $f_c$ , water vapor concentrations,  $e_a$  (as a measure of the total water vapor content  
84 of the atmospheric column), and air temperature,  $T_a$  (as a proxy for the heat storage within the lower-level  
85 atmosphere, Panwar et al. 2022 as a proxy for the total atmospheric heat storage within the column). With  
86 this, we can then attribute variations in  $R_{ld}$  to their physical causes.

87 Here, our aim is to first evaluate this estimate for downwelling longwave radiation with current global  
88 datasets at the continental scale. These variations are illustrated using the NASA-CERES (EBAF 4.1)  
89 dataset (Loeb et al., 2018; Kato et al., 2018, NASA/LARC/SD/ASDC 2017) and the NASA-CERES  
90 Syn1deg dataset (Doelling et al., 2013, 2016) in Figure 1 and are compared to variations in solar radiation.  
91 It can be seen that the climatological distribution of  $R_{ld}$  is mostly associated with latitudes, while also  
92 presenting some zonal variations, e.g., across western and eastern North America. In comparison, the  
93 seasonal cycle of  $R_{ld}$  is less determined by latitudes (Fig. 1b). It has a larger magnitude over land than over  
94 oceans, over arid regions than humid regions, and over cold regions more than over warm ones. Although  
95 studies have revealed a close correlation between the variation of  $R_{ld}$  and other factors like air temperature,  
96 water vapor, and  $\text{CO}_2$  concentration (Wang and Liang 2009; Wei et al. 2021), here we go beyond  
97 correlations and rather attribute these variations to the different terms in Eqns. (1)-(5) that represent  
98 different radiative properties affecting  $R_{ld}$ .

99 To figure out the dominant driver for these spatiotemporal variations, we decompose changes in  $R_{ld}$  into its  
100 components: cloud cover,  $f_c$ , heat storage changes of atmosphere as reflected by 2m air temperature,  $T_a$ ,  
101 and air humidity,  $e_a$ , by performing the differentiation of these equations. We show that heat storage  
102 changes predominantly shape the diurnal range and seasonal cycle of  $R_{ld}$ , while cloud cover variations play  
103 a second role in most cases. In addition, the temporal variations of  $R_{ld}$  are less over the ocean than over  
104 land, and less during winter than summer. On the other hand, the spatial variations of  $R_{ld}$  from arid to humid  
105 regions is relatively small, which we will show is due to a compensating effect of corresponding changes  
106 in atmospheric emissivity and heat storage.

107 Our paper is organized as follows: After briefly describing the datasets used in our evaluation in Section 2,  
108 we first estimate of  $R_{ld}$  from these equations at the global scale, using multiple datasets in Section 3.1.  
109 After showing that the annual-mean and large-scale variations are well captured, we then use the equations  
110 to decompose the temporal variations of  $R_{ld}$  in terms of its mean spatial and temporal variations and relate  
111 these to their causes in Section 3.2. The spatial variations of  $R_{ld}$  are then further discussed in Section 3.3 in  
112 terms of its relationship with aridity. We then close with a brief summary and broader implications.

## 113 2 Datasets

114 To test  $R_{ld}$  estimates, we use FLUXNET [half-hour](#) observations (Pastorello et al. 2020, half-hourly values,  
115 189 sites, see Table S1 [and Figure S2](#) for details), the NASA-CERES [monthly](#) satellite-based radiation  
116 dataset (Doelling et al., 2013, 2016, monthly means, covering years 2001 to 2018), and the ERA5 [monthly](#)  
117 reanalysis dataset (Hersbach et al. 2018, monthly means, covering years 1979 to 2021).

118 For each dataset,  $T_a$ ,  $e_a$ , and  $f_c$  are needed as inputs for Eqs. (1)-(5), while  $R_{ld}$  data is used for the  
119 comparison. ~~Cloud cover  $f_c$  is calculated using Eq. (3) for all three datasets with incoming solar radiation  
120 at the surface ( $R_s$ ) and the potential solar radiation ( $R_{s,pot}$ ). Cloud cover  $f_c$  is calculated using Eq. (3) for  
121 all three datasets with incoming solar radiation at the surface ( $R_s$ ) and the potential solar radiation ( $R_{s,pot}$ ).~~

122 For NASA-CERES estimation,  $T_a$  from the CPC Global Unified Temperature dataset (CPC Global Unified  
123 Temperature) is used as temperature observation.

124 For all three datasets, water vapor pressure,  $e_a$ , is not directly given. It is calculated from the water vapor  
125 deficit (VPD, FLUXNET) or dewpoint temperature ( $T_{dew}$ , ERA5) using Monteith and Unsworth (2008):

$$e_a = 6.1079 \times \exp(17.269T_{dew}/(237.3 + T_{dew})), \quad (6)$$

$$e_a = 6.1079 \times \exp(17.269T_a/(237.3 + T_a)) - VPD, \quad (7)$$

126 And the calculated  $e_a$  from ERA5 is also used in NASA-CERES estimation.

127 For the analysis of the spatial variations of  $R_{ld}$  along water availability, we use the aridity index ( $AI = \frac{R}{LP}$ )  
128 (Budyko 1958; UNCOD 1977). This index is calculated using the mean annual net radiation ( $R$ ) taken from  
129 the NASA-CERES dataset, the mean annual net precipitation ( $P$ ) taken from the CPC Global Unified  
130 Gauge-Based Analysis of Daily Precipitation data (Chen et al. 2008 and Xie et al. 2007, CPC Global Unified  
131 Gauge-Based Analysis of Daily Precipitation), and a latent heat of vaporization for water of  $L =$   
132 2260 kJ/kg. A larger value of  $AI$  indicates stronger aridity.

### 133 3 Results and discussion

#### 134 3.1 Comparison to observed, satellite, and reanalysis data

135 We first compared the estimates of  $R_{ld}$  at a point-by-point basis separately for clear-sky and all-sky  
136 conditions using Eqns. (2) and (5), respectively. This comparison is shown in Figure 2 using FLUXNET,  
137 CERES, and ERA5 data. The estimates correlate very well with  $r^2$  of 0.92 and 0.87 for clear sky and all-  
138 sky conditions, respectively, and RMSE values of 18.24 and 24.56  $W m^{-2}$ . The slope of the linear  
139 regressions between the estimated and observed  $R_{ld}$  for FLUXNET are 1.03 and 1.02, with most data points  
140 being concentrated around the 1:1 line (Figs. 2a and 2b). The estimates correlate very well with  $r^2$  of 0.92  
141 and 0.87 for clear-sky and all-sky conditions, respectively, and RMSE values of 18.24 and 24.56  $W m^{-2}$ .  
142 The slope of the linear regressions between the estimated and observed  $R_{ld}$  for FLUXNET are 1.03 and  
143 1.02, with most data points being concentrated around the 1:1 line (Figs. 2a and 2b). Note that for all-sky  
144 conditions, the agreement is slightly less good, with a lower correlation coefficient and a larger RSME. The  
145 agreement with the NASA-CERES and ERA5 datasets are even better, with higher correlation coefficients  
146 and lower RSME.

147 Despite this high level of agreement of the estimates, we can see some systematic biases in the estimates  
148 for  $R_{ld}$ . These can be seen in Figure 3 and Figure S2, which show the spatial distribution of these bias and  
149 their links with temperature and humidity. For clear sky conditions, there appears to be a general  
150 underestimation in the high latitudes and, to some extent, in arid regions (Figs. 3e and 3e). This bias can be  
151 attributed to biases in the equations used here. Brutsaert (1975) already described that for very low  
152 temperatures and in arid conditions, there are better parameter values than those used in Eq. 1, with a larger  
153 coefficient than 1.24 and a different exponent, which thus leading to an underestimation under low humidity  
154 (Figs. 3a, S2a, S2e). Moreover, B75 has not considered the gradual increase in emissivity as temperature  
155 decreases below freezing (Aase and Idso 1978), thus explaining the underestimation under low temperature  
156 (Figs. 3b, S2b, S2b). The biases seen in Figure 3 are nevertheless notably smaller than the spatial temporal  
157 variations shown in Figure 1, this means that these biases do not prevent us from using Brutsaert to attribute  
158 the causes for the seasonal variation and the spatial range of  $R_{ld}$ .

159 The biases for all sky conditions generally share the distribution with that of clear sky conditions, with a  
160 smaller magnitude (Figs. 3b, 3d and 3f), which are also small compared to the spatial temporal variations.

161 These can be seen in Figure 3 and Figure S3, which show the spatial distribution of these biases and their  
162 variations against temperature and humidity. For clear-sky conditions, there appears to be a general  
163 underestimation in the high latitudes and, to some extent, in arid regions (Figs. 3c and 3e). Brutsaert (1975)  
164 already described that for very low temperatures and in arid conditions, there are better parameter values

格式化表格

设置了格式: 字体: 非倾斜

165 than those used in Eq. 1, with a larger coefficient than 1.24 and a different exponent. This can then, which  
 166 thus leading to an underestimation of  $R_{ld}$  under low humidity (Figs. 3a, S3a, S3c). Moreover, B75 has not  
 167 considered the gradual increase in emissivity as temperature decreases below freezing (Aase and Idso  
 168 1978), thus explaining the underestimation under low temperature (Figs. 3b, S3b, S3b). The biases seen in  
 169 Figure 3 are nevertheless notably smaller than the spatial-temporal variations shown in Figure 1. This  
 170 means that these biases do not prevent us from using Brutsaert to attribute the causes for the seasonal  
 171 variation and the spatial range of  $R_{ld}$ .

172 The biases for all-sky conditions generally share the distribution with that of clear-sky conditions, with a  
 173 smaller magnitude (Figs. 3b, 3d and 3f), which are also small compared to the spatial-temporal variations.

174 Overall, this evaluation shows that the expressions given by Eqns. (1) - (5) are very well suited to describe  
 175 the spatiotemporal variations of  $R_{ld}$  for current climatological conditions.

### 177 3.2 Attribution of diurnal and seasonal variations

178 We next use Eqns. (1) - (5) to attribute temporal variations of  $R_{ld}$  to their physical causes. To do so, we can  
 179 express changes  $\Delta R_{ld}$  as a function of changes in water vapor,  $\Delta e_a$ , cloud cover,  $\Delta f_c$ , and air temperature,  
 180  $\Delta T_a$ . The functional dependence is derived from the equations by differentiation and applying the chain  
 181 rule. In a first step, we express a change  $\Delta R_{ld}$  by the partial contributions  $\Delta R_{ld,\varepsilon}$  and  $\Delta R_{ld,T}$ , that are due to  
 182 changes in emissivity,  $\Delta\varepsilon$ , and due to changes in atmospheric heat storage that are associated with a change  
 183 in air temperature  $\Delta T_a$ :

$$\Delta R_{ld} = \Delta R_{ld,\varepsilon} + \Delta R_{ld,T} = \frac{\partial R_{ld}}{\partial \varepsilon} \Delta \varepsilon + \frac{\partial R_{ld}}{\partial T_a} \Delta T_a = \sigma \bar{T}_a^4 \Delta \varepsilon + 4\sigma \bar{\varepsilon} \bar{T}_a^3 \Delta T_a. \quad (8)$$

184 The 2 terms at the right side of Eq. 8 are  $\Delta R_{ld,\varepsilon}$  and  $\Delta R_{ld,T}$ , respectively.

185 The contribution  $\Delta R_{ld,\varepsilon}$  is further decomposed into contributions  $\Delta R_{ld,f_c}$ ,  $\Delta R_{ld,e_a}$ , and  $\Delta R_{ld,T_a'}$  due to  
 186 variations in clouds,  $\Delta f_c$ , air humidity,  $\Delta e_a$ , and surface temperature,  $\Delta T_a$ . We obtain:

$$\begin{aligned} \Delta R_{ld,\varepsilon} &= \sigma \bar{T}_a^4 \Delta \varepsilon \approx \sigma \bar{T}_a^4 \times \frac{\partial \varepsilon}{\partial f_c} \Delta f_c + \sigma \bar{T}_a^4 \times \frac{\partial \varepsilon}{\partial e_a} \Delta e_a + \sigma \bar{T}_a^4 \times \frac{\partial \varepsilon}{\partial T_a} \Delta T_a \\ &= \sigma \bar{T}_a^4 \times \left( 1 - 1.24 \left( \frac{\bar{e}_a}{\bar{T}_a} \right)^{\frac{1}{7}} \right) \Delta f_c + \sigma \bar{T}_a^4 \times \frac{1.24}{7} \frac{(1 - \bar{f}_c)}{(\bar{e}_a)^{\frac{6}{7}} (\bar{T}_a)^{\frac{1}{7}}} \Delta e_a \\ &\quad + \sigma \bar{T}_a^4 \times \left( -\frac{1.24}{7} \right) \times \frac{(1 - \bar{f}_c) (\bar{e}_a)^{\frac{1}{7}}}{(\bar{T}_a)^{\frac{8}{7}}} \times \Delta T_a \end{aligned} \quad (9)$$

187 The 3 terms at the right side of Eq. 9 are  $\Delta R_{ld,f_c}$ ,  $\Delta R_{ld,e_a}$ , and  $\Delta R_{ld,T_a'}$ , respectively.

188 Note that the third term is of less magnitude compared with the other two terms (e.g. in terms of the  
 189 seasonal range as shown in Fig. 5f), which is hence not focused in this work.

190 We next applied this approach to the diurnal deviations  $\Delta R_{ld}$  from the daily mean using the FLUXNET  
 191 dataset. This decomposition is shown in Figure 4 in aggregated form across the FLUXNET sites for whole  
 192 year (Fig. 4a), the Northern hemisphere summer (Fig. 4b) and winter seasons (Fig. 4c). More than 95% of  
 193 the diurnal variations (of about  $\pm 20 \text{ W m}^{-2}$ ) are primarily caused by diurnal changes in air temperature,  
 194 while variations in emissivity play practically no role (Fig. S4). Diurnal changes in air temperature reflect  
 195 variations in heat storage of the atmospheric boundary layer. This is consistent with the notion that diurnal  
 196 variations in solar radiation over land are buffered primarily by the lower atmosphere, rather than below  
 197 the surface as it is the case for open water bodies and the ocean (Kleidon and Renner 2017). Since most of

设置了格式: 字体: (中文)+中文正文 (宋体), (中文) 简体中文(中国大陆)

设置了格式: 字体: 非倾斜

设置了格式: 字体: (中文)+中文正文 (宋体), 英语(英国)

198 the stations in the FLUXNET dataset are located in the midlatitudes of the Northern hemisphere, the  
199 variations are consistently larger in summer due to the greater solar input (Fig. 4b) than in winter (Fig. 4c).

200 Figure 5 shows the same kind of decomposition, but for seasonal variations in  $R_{ld}$  in the NASA-CERES  
201 dataset, which is the difference between the maximum and minimum of monthly  $R_{ld}$  data shown in Fig. S3.  
202 ~~The aggregation to the global scale across land and ocean is also shown in Fig. S3, where the deviations~~  
203 ~~are calculated as the difference of the monthly means to the annual mean.~~ Generally, areas with relatively  
204 low annual-mean  $R_{ld}$ , e.g. the high latitude regions of North America and northeastern Eurasia, have the  
205 largest seasonal cycle (Fig. 1). ~~The decomposition shows that this variation is mostly due to the seasonal~~  
206 ~~variation in atmospheric heat storage ( $\Delta R_{ld,T}$ ), with a portion of around 73% on a global scale, and the rest~~  
207 ~~are attributed to the seasonal changes in water vapor (24%) and cloud cover (12%).~~ ~~The decomposition shows~~  
208 ~~that this variation is mostly due to the seasonal variation in atmospheric heat storage ( $\Delta R_{ld,T}$ ), with a portion~~  
209 ~~of around 73% on a global scale, and the rest are attributed to the seasonal changes in water vapor (24%)~~  
210 ~~and cloud cover (12%).~~ ~~Notably, seasonal variations in emissivity play a greater role than atmospheric heat~~  
211 ~~storage in changing  $R_{ld}$  in tropical areas, especially over the monsoon region, and this is predominantly due~~  
212 ~~to seasonal fluctuations in water vapor levels (Figs. 5d-5f).~~ ~~Notably, seasonal variations in emissivity play~~  
213 ~~a greater role than atmospheric heat storage in changing  $R_{ld}$  in tropical areas, especially over the monsoon~~  
214 ~~region, and this is predominantly due to the strong seasonal fluctuations in water vapor levels and cloud-~~  
215 ~~cover (Figs. 5d-5f).~~

216 ~~The aggregation to the global scale across land and ocean is shown in Fig. S5, where the deviations are~~  
217 ~~calculated as the difference of the monthly means to the annual mean.~~ Figs. S5 show that the seasonal  
218 variations of  $R_{ld}$  is generally less over the ocean than on the land, an effect that can also be seen in Fig. 1.  
219 The decomposition shows that these variations are mostly caused by changes in ~~lower-level~~ atmospheric  
220 heat storage, with a slight modulation by emissivity changes. This can, again, be largely explained by the  
221 effect described above for the diurnal variations (Kleidon and Renner 2017). ~~Over the land, the changes in~~  
222 ~~radiation are majorly buffered by the heat storage in the lower atmosphere by the variations in convective~~  
223 ~~boundary layer height. However, over marine areas, solar radiation penetrates the transparent water bodies,~~  
224 ~~the heat storage of which hence buffers the season cycle of the radiation over the ocean. Since the heat~~  
225 ~~storage of the water body is larger than that of the lower atmospheric boundary layer, the buffering effect~~  
226 ~~is consequently larger, which leads to the less seasonal cycle of the surface temperature and  $R_{ld}$  over the~~  
227 ~~ocean.~~ ~~Over the land, the changes in radiation are majorly buffered by the heat storage in the lower~~  
228 ~~atmosphere by the variations in convective boundary layer height. However, over marine areas, solar~~  
229 ~~radiation penetrates the transparent water bodies, the heat storage of which hence buffers the season cycle~~  
230 ~~of the radiation over the ocean. Since the heat storage of the water body is larger than that of the lower~~  
231 ~~atmospheric boundary layer, the buffering effect is consequently larger, which leads to the less seasonal~~  
232 ~~cycle of the surface temperature and  $R_{ld}$  over the ocean.~~

233 In summary, what our decomposition shows is that most temporal variations in  $R_{ld}$  in current, climatological  
234 conditions are explained by heat storage changes within the lower atmosphere.

### 235 236 3.3 Attribution of geographic variations with aridity

237 Last, we applied the decomposition to the climatological variations in  $R_{ld}$  along with differences in mean  
238 water availability. Water availability was characterized by Budyko's aridity index (AI), with values  $AI <$   
239  $1$  representing humid regions, and larger values reflecting increased aridity. ~~The spatial distribution of AI~~  
240 ~~is shown in Fig. S6~~ ~~The spatial distribution of AI is shown in Fig. S7.~~ Here, the deviations  $\Delta R_{ld}$  are  
241 calculated with respect to the ~~global~~ annual mean ~~over land~~. The different contributions to the deviations  
242 are shown in Fig. 6, as well as the delineation along the aridity index (Figs. 6e - f).

243 ~~The decomposition of the spatial distribution of the climatological means shows that the variations are~~  
244 ~~largely caused by differences in atmospheric heat storage as well (Fig. 6a). The contribution due to~~

245 variations in emissivity has a much smaller magnitude (Fig. 6b), and is dominated by changes in cloud  
246 cover (Fig. 6c) and changes in water vapor (Fig. 6d) at high- and mid- latitudes respectively.

247 The decomposition of the spatial distribution of the climatological means shows that the variations are  
248 largely caused by differences in lower-level atmospheric heat storage as well (Fig. 6a). The contribution  
249 due to variations in emissivity has a smaller magnitude (Fig. 6b), and is dominated by changes in cloud  
250 cover (Fig. 6c) and changes in water vapor (Fig. 6d) at high- and mid- latitudes respectively.

251 These variations are evaluated with respect to the aridity index in Figs. 6e, 6-f and S7. While there is a  
252 large spread, as seen in the quantiles, there is a small, but consistent trend towards lower values of  $R_{ld}$  in  
253 more arid regions, with a magnitude of about  $-10\sim 20\text{ W m}^{-2}$  across the entire aridity index spectrum across  
254 the entire aridity index spectrum (black dashed line in Figs. 6e and 6f). We also notice a shift in the  
255 contributions, with emissivity contributing less and lower-level atmospheric heat storage contributing more  
256 with increased values of AI. The changes decreasing contributions in emissivity of about  $-20\sim 40\text{ W m}^{-2}$   
257 is caused by reductions in cloud cover and water vapor (as shown by the orange lines in Figs. 6f), and  
258 amounts to around  $-40\text{ W m}^{-2}$  over the range shown in the Figure 6e which. This decrease in cloud cover  
259 and water vapor can be attributed to the common presence of high-pressure systems in subtropical arid  
260 areas (Zampieri et al. 2009) and less monsoon there. The decreasing contribution by lower atmospheric  
261 emissivity is compensated for by an increased contribution of about  $+10\sim 20\text{ W m}^{-2}$  by atmospheric heat  
262 storage that is caused by the generally warmer mean temperatures in arid regions.

263 Taken together, these trends imply that, again, the climatological variations in  $R_{ld}$  are also dominated by  
264 differences in atmospheric heat storage. A small, but consistent change can be seen in the contributions  
265 along the aridity index, with the contribution by emissivity due to cloud cover becoming lower while the  
266 contribution by atmospheric heat storage increases as regions become drier.

#### 267 4. Discussion and Conclusions

268 We found that the semiempirical equations of Brutsaert (1975) and Crawford and Duchon (1999) work very  
269 well to estimate the downwelling flux of longwave radiation by comparing these to estimates from  
270 observation, satellite, and reanalysis datasets, with  $r^2$  ranging from 0.87 to 0.98 across the datasets for clear-  
271 sky and all-sky conditions with  $r^2$  ranging from 0.87 to 0.98 across the datasets for clear-sky and all-sky  
272 conditions. We then showed that one can use these equations to decompose this flux into different  
273 components, and relate changes to differences in cloud cover, water vapor, and lower-level atmospheric  
274 heat storage. We found that most diurnal changes in downwelling longwave radiation are caused by  
275 differences in lower-level atmospheric heat storage that are reflected in differences in surface air  
276 temperature, with the changes in atmospheric emissivity playing the second role. The dominance of surface  
277 air temperature can be also observed in the seasonal range in  $R_{ld}$ , except in tropical monsoon regions due  
278 to large variations of water vapor. As for the spatial variation, from arid to humid region, the increasing  
279 lower-level atmospheric heat storage and decreasing atmospheric emissivity have an offsetting effect on the  
280  $R_{ld}$  variation, thus leading to relatively subtle changes in  $R_{ld}$  along with aridity index. We found that most  
281 diurnal changes in downwelling longwave radiation are caused by differences in lower-level atmospheric  
282 heat storage that are reflected in differences in surface air temperature, with the changes in atmospheric  
283 emissivity playing the secondary role. The dominance of surface air temperature can be also observed in  
284 the seasonal ranges of  $R_{ld}$ , except in tropical monsoon regions due to large variations in water vapor and  
285 cloud cover. As for the spatial variation, from arid to humid region, the increasing lower-level atmospheric  
286 heat storage and decreasing atmospheric emissivity have an offsetting effect on the  $R_{ld}$  variation, thus  
287 leading to relatively subtle changes in  $R_{ld}$  along with aridity index.

289  
290 Relating our decomposition to radiative kernel helps to gain a more comprehensive understanding of  
291 variations in  $R_{ld}$ . Referring to the sensitivity in the downwelling longwave radiation for an incremental

设置了格式: 字体: (中文) + 中文正文 (宋体)

带格式的: 段落间距段前: 6 磅, 段后: 0 磅, 行距: 单倍行距

292 change in an atmospheric property (e.g.,  $T_a$ ,  $f_c$ , and  $e_a$ ), radiative kernel has been used to attribute  $R_{ld}$   
 293 changes, based on numerically calculation with radiative transfer code (Previdi 2010 and Vargas Zeppetello  
 294 et al. 2019) or partial differentiating with explicit formula for  $R_{ld}$  (Shakespeare and Roderick, 2022).  
 295 Following Shakespeare and Roderick (2022), the approximate radiative kernel of  $T_a$ ,  $f_c$ , and  $e_a$  are calculated

296 based on Eqs. 8-9 ( i.e.,  $\frac{\partial R_{ld}}{\partial T} = 4\sigma\bar{\epsilon}T_a^{-3} \frac{\partial R_{ld}}{\partial f_c} = \sigma T_a^{-4} \times \left(1 - 1.24 \left(\frac{e_a}{T_a}\right)^{\frac{1}{7}}\right)$ , and  $\frac{\partial R_{ld}}{\partial e_a} = \sigma T_a^{-4} \times \frac{1.24}{7} \frac{(1-f_c)}{(e_a)^{\frac{6}{7}}(T_a)^{\frac{1}{7}}}$ )

297 and shown in the left panel of Fig. S8. As shown in Fig S8a,- the sensitivity of  $R_{ld}$  to  $T_a$  peaks in the tropics  
 298 with a maximum of around 5 W/m<sup>2</sup>/K and decreases at higher latitudes, which is generally consistent with  
 299 Shakespeare & Roderick (2022). Moreover, the seasonal cycle of the atmospheric properties themselves  
 300 are shown in the right panel of Figure S8, which reveals that the spatial distribution of the contribution of  
 301  $T_a$ ,  $e_a$ , and  $f_c$  to the seasonal variations in  $R_{ld}$  (Figure 5) is dominated by the seasonal changes of the air  
 302 properties (Figs. S8b, S8d, and S8f) instead of the sensitivity of  $R_{ld}$  to them (Figs. S8a, S8c, and S8e).

303 Relating our decomposition to radiative kernel helps to gain a more comprehensive understanding of  
 304 variations in  $R_{ld}$ . Referring to the sensitivity in the downwelling longwave radiation for an incremental  
 305 change in an atmospheric property (e.g.,  $T_a$ ,  $f_c$ , and  $e_a$ ), radiative kernel has been used to attribute  $R_{ld}$   
 306 changes, based on numerically calculation with radiative transfer code (Previdi 2010 and Vargas Zeppetello  
 307 et al. 2019) or partial differentiating with explicit formula for  $R_{ld}$  (Shakespeare and Roderick, 2022).  
 308 Following Shakespeare and Roderick (2022), the approxiamate radiative kernel of  $T_a$ ,  $f_c$ , and  $e_a$  are

309 calculated ( i.e.,  $\frac{\partial R_{ld}}{\partial T} = 4\sigma\bar{\epsilon}T_a^{-3} \frac{\partial R_{ld}}{\partial f_c} = \sigma T_a^{-4} \times \left(1 - 1.24 \left(\frac{e_a}{T_a}\right)^{\frac{1}{7}}\right)$ , and  $\frac{\partial R_{ld}}{\partial e_a} = \sigma T_a^{-4} \times \frac{1.24}{7} \frac{(1-f_c)}{(e_a)^{\frac{6}{7}}(T_a)^{\frac{1}{7}}}$ ) and

310 shown in Fig. S6 ( i.e.,  $\frac{\partial R_{ld}}{\partial T} = 4\sigma\bar{\epsilon}T_a^{-3} \frac{\partial R_{ld}}{\partial f_c} = \sigma T_a^{-4} \times \left(1 - 1.24 \left(\frac{e_a}{T_a}\right)^{\frac{1}{7}}\right)$ , and  $\frac{\partial R_{ld}}{\partial e_a} = \sigma T_a^{-4} \times \frac{1.24}{7} \frac{(1-f_c)}{(e_a)^{\frac{6}{7}}(T_a)^{\frac{1}{7}}}$ ),

311 together with the seasonal range of the atmospheric property themselves. As shown in Fig S4, the radiative

312 These equations can then be applied to different aspects of climate research.- For instance, the values of  
 313 downwelling longwave radiation are often missing in FLUXNET data (Table S2), and these equations can  
 314 be used to fill the gaps with air temperature and humidity observations. We can also use these equations to  
 315 better understand the physical mechanisms for temperature change due to extreme events. For instance,  
 316 Park et al. (2015) and Alekseev et al. (2019) found that an enhancement of downwelling longwave radiation  
 317 in the Arctic is found to be preceded by the advection of moisture and heat. -The equations by Brutsaert  
 318 (1975) and Crawford and Duchon (1999) can then be used to quantify the individual contributions by the  
 319 advection of heat and moisture (Tian et al. 2022).- Another example is the attribution of differences in  
 320 temperatureglobal warming magnitudes across humid and arid regions (Ghausi et al., 2023). Du et al.  
 321 (2020) used these equations to explain why global warming was stronger during clear-sky conditions in  
 322 observations in China due to the greater sensitivity of clear-sky emissivity to a change in water vapor. This  
 323 was then used to explain the observed, stronger global warming in the arid regions of China, which have  
 324 less clouds and a higher frequency of clear-sky conditions than the humid regions. Furthermore, -wWhile  
 325 the empirical coefficient of 1.24 in Eq. (1) may change due to emissivity changes from greenhouse gases  
 326 other than water vapor, this formulation can nevertheless provide a useful basis in terms of the interannual  
 327 changes of  $R_{ld}$ , which is shown in Fig. S9. As shown in Fig. S9a,  $R_{ld}$  increases in most of the land regions,  
 328 at an average rate of 0.64 W/m<sup>2</sup>/decade, with the contribution of increased temperature, increased water  
 329 vapor, and decreased cloud cover contributing 0.46, 0.28, -0.10 W/m<sup>2</sup>/decade, respectively. Furthermore,  
 330 it can be observed in Figs. S9d-S9j that the temperature effect is generally around 0.5 W/m<sup>2</sup>/decade, while  
 331 the influence of emissivity is significantly dominant in the monsoon region, which is majorly due to the  
 332 interannual changes in water vapor.-

333 It is worth noting that several effects on  $R_{ld}$  variations are not included in B75 and C&D99, e.g., the well-  
 334 mixed greenhouse gas concentrations (Shakespeare and Roderick, 2022), large aerosol particles (Zhou and  
 335 Savijärvi, 2013), and cloud base (Viúdez-Mora et al. 2015). Although rarely influencing the diurnal change,

- 设置了格式: 下标
- 设置了格式: 字体: 11 磅, 非倾斜
- 设置了格式: 字体: 11 磅
- 设置了格式: 字体: 11 磅, 非倾斜
- 设置了格式: 字体: 11 磅
- 设置了格式: 字体: 11 磅, 非倾斜
- 设置了格式: 字体: 11 磅, 非倾斜



336 seasonal cycles, and spatial distribution, these terms needs attention when the interannual trend of Rld is  
337 investigated under global warming, which can be implied by the difference between Figs. S9a and S9b. In  
338 addition, B75 in conjunction with C&D99 is adopted in this work to decompose the Rld variations in  
339 different spatial-temporal scales, considering its solid physical foundations and the relatively less  
340 computation consumption. Further analysis can be performed based on other estimations, e.g. Prata 1996,  
341 which shows consistency with reanalysis data (Allan et al. 2004). The cloud effect can be also detected  
342 using the difference between all-sky and clear-sky Rld (Allan 201; Ghausi et al., 2022). Moreover, datasets  
343 that are more focused on radiation and energy budget can be used to test the robust of the results, e.g.,  
344 BSRN (Driemel et al. 2018) and GEBA (Wild et al. 2017).

设置了格式: 字体: 11 磅

设置了格式: 字体: 11 磅

设置了格式: 字体: 11 磅

设置了格式: 字体: 11 磅

设置了格式: 字体: 11 磅, 非倾斜

设置了格式: 字体: 11 磅

345 ~~We conclude that the equations by Brutsaert (1975) and Crawford and Duchon (1999) are still very useful~~  
346 ~~to advance our understanding of surface temperature changes.~~ We conclude that the equations by Brutsaert  
347 (1975) and Crawford and Duchon (1999) are still very useful ~~to advance~~in advancing our understanding of  
348 surface temperature changes.- Our evaluation has shown how well these equations estimate this flux, and  
349 our application to the decomposition of different contributions has shown its utility ~~to understand~~in  
350 understanding the causes ~~for~~of its variation. -These equations should help us to better understand aspects of  
351 climate variability, extreme events, and global warming, linking these to the mechanistic contributions by  
352 downwelling longwave radiation.

设置了格式: 字体: 小四, 英语(英国), 图案: 清除 (白色)

## 353 Acknowledgments

354 This research is supported by the National Natural Science Foundation of China (52209026) and the Second  
355 Tibetan Plateau Scientific Expedition and Research Program (grant no. 2019QZKK0208). This research  
356 resulted from a research stay of YLT in AK's research group. This stay was supported by China Scholarship  
357 Council as No. 202106210161. AK and SAG acknowledge funding from the Volkswagen Stiftung through  
358 the ViTamins project.

## 359 Author contributions

360 YLT, SAG, and AK conceived and designed the analysis, with inputs from DZ and GW. YLT performed  
361 the analysis and discussed the results with all authors. YLT and AK wrote the paper.

## 362 Competing interests

363 The contact author has declared that none of the authors has any competing interests.

设置了格式: 字体: 11 磅, 字体颜色: 文字 1, (中文) 简体中文(中国大陆), (其他) 英语(美国)

## 364 Data availability

365 The data used in this study was downloaded from the links provided with the references. No new data was  
366 created.

## References

- 368 Aase, J. K., and S. B. Idso, 1978: A comparison of two formula types for calculating long-wave radiation from the atmosphere.  
 369 Water Resources Research, 14, 623-625. <https://doi.org/10.1029/WR014i004p00623>  
 370  
 371  
 372 Alados, I., I. Foyo-Moreno, and L. Alados-Arboledas, 2012: Estimation of downwelling longwave irradiance under all-sky  
 373 conditions. International Journal of Climatology, 32, 781-793. <https://doi.org/10.1002/joc.2307>  
 374  
 375 [Allan, R. P., Ringer, M. A., Pamment, J. A., and Slingo, A. \(2004\). Simulation of the Earth's radiation budget by the European  
 376 Centre for Medium-Range Weather Forecasts 40-year reanalysis \(ERA40\), J. Geophys. Res., 109, D18107,  
 377 <https://doi.org/10.1029/2004JD004816>](#)  
 378  
 379 Alekseev, G., S. Kuzmina, L. Bobylev, A. Urazgildeeva, and N. Gnatiuk, 2019: Impact of atmospheric heat and moisture transport  
 380 on the Arctic warming. Int. J. Climatol., 39, 3582-3592, <https://doi.org/10.1002/joc.6040>.  
 381  
 382 Budyko, M. I. (1958) The Heat Balance of the Earth's Surface, trs. Nina A. Stepanova, US Department of Commerce, Washington,  
 383 D.D., 259 p.  
 384  
 385 Brutsaert, W., 1975: On a derivable formula for long-wave radiation from clear skies. Water Resources Research, 11, 742-744.  
 386 <https://doi.org/10.1029/WR011i005p00742> .  
 387  
 388 Crawford, T. M., and C. E. Duchon, 1999: An Improved Parameterization for Estimating Effective Atmospheric Emissivity for  
 389 Use in Calculating Daytime Downwelling Longwave Radiation. Journal of Applied Meteorology, 38, 474-480.  
 390 [https://doi.org/10.1175/1520-0450\(1999\)038<0474:Aipfee>2.0.Co;2](https://doi.org/10.1175/1520-0450(1999)038<0474:Aipfee>2.0.Co;2)  
 391  
 392 Chen, M., W. Shi, P. Xie, V. B. S. Silva, V. E. Kousky, R. Wayne Higgins, and J. E. Janowiak (2008), Assessing objective  
 393 techniques for gauge-based analyses of global daily precipitation, J. Geophys. Res., 113, D04110, >),  
 394 <https://doi.org/10.1029/2007JD009132>.  
 395  
 396 CPC Global Unified Temperature. Available online: <https://psl.noaa.gov/data/gridded/data.cpc.globaltemp.html>, provided by the  
 397 NOAA PSL, Boulder, Colorado, USA, from their website at <https://psl.noaa.gov> (accessed on 6 March 2022).  
 398  
 399 CPC Global Unified Gauge-Based Analysis of Daily Precipitation. Available online:  
 400 <https://psl.noaa.gov/data/gridded/data.cpc.globalprecip.html>, provided by the NOAA PSL, Boulder, Colorado, USA, from their  
 401 website at <https://psl.noaa.gov> (accessed on 5 March 2022)  
 402  
 403 [Driemel, A., Augustine, J., Behrens, K., Colle, S., et al. \(2018\) Baseline Surface Radiation Network \(BSRN\): structure and data  
 404 description \(1992–2017\), Earth Syst. Sci. Data, 10, 1491–1501, <https://doi.org/10.5194/essd-10-1491-2018> .](#)  
 405  
 406 Du, M., Kleidon, A., Sun, F., Renner, M., & Liu, W. (2020). Stronger global warming on nonrainy days in observations from  
 407 China. Journal of Geophysical Research: Atmospheres, 125, e2019JD031792. <https://doi.org/10.1029/2019JD031792>  
 408  
 409 Doelling, D. R., Loeb, N. G., Keyes, D. F., Nordeen, M. L., Morstad, D., Nguyen, C., and Sun, M.: Geostationary enhanced  
 410 temporal interpolation for CERES flux products, J. Atmos. Ocean. Tech., 30, 1072–1090, 2013.  
 411  
 412 Doelling, D. R., Sun, M., Nguyen, L. T., Nordeen, M. L., Haney, C. O., Keyes, D. F., and Mlynczak, P. E.: Advances in  
 413 geostationary-derived longwave fluxes for the CERES synoptic (SYN1 deg) product, J. Atmos. Ocean. Tech., 33, 503–521, 2016.  
 414  
 415 Duarte, H. F., N. L. Dias, and S. R. Maggionto, 2006: Assessing daytime downward longwave radiation estimates for clear and  
 416 cloudy skies in Southern Brazil. *Agricultural and Forest Meteorology*, **139**, 171-181.  
 417 <https://doi.org/10.1016/j.agrformet.2006.06.008>  
 418  
 419 Flerchinger, G. N., W. Xaio, D. Marks, T. J. Sauer, and Q. Yu, 2009: Comparison of algorithms for incoming atmospheric long-  
 420 wave radiation. *Water Resources Research*, **45**, <https://doi.org/10.1029/2008WR007394>  
 421  
 422 [Ghausi, S. A., Tian Y., Zehe E., & Kleidon A. \(2023\) Radiative controls by clouds and thermodynamics shape surface temperatures  
 423 and turbulent fluxes over land. Proceedings of the National Academy of Sciences, 120 \(29\), e2220400120,  
 424 <https://doi.org/10.1073/pnas.2220400120>](#)  
 425

域代码已更改

设置了格式: 字体颜色: 文字 1

域代码已更改

域代码已更改

域代码已更改

域代码已更改

域代码已更改

域代码已更改

域代码已更改

域代码已更改

域代码已更改

域代码已更改

426 [Ghausi, S. A., Ghosh, S., & Kleidon, A. \(2022\). Breakdown in precipitation–temperature scaling over India predominantly](#)  
427 [explained by cloud-driven cooling. \*Hydrology and Earth System Sciences\*, 26\(16\), 4431–4446.](#)

428

429 Hatfield, J. L., R. J. Reginato, and S. B. Idso, 1983: Comparison of long-wave radiation calculation methods over the United States.  
430 *Water Resources Research*, 19, 285–288. <https://doi.org/10.1029/WR019i001p00285>

431

432 Held, I. M., and B. J. Soden, 2000: Water Vapor Feedback and Global Warming. *Annual Review of Energy and the Environment*,  
433 25, 441–475.

434

435 Hersbach, H., and Coauthors, 2018: ERA5 hourly data on single levels from 1959 to present. Copernicus Climate Change Service  
436 (C3S) Climate Data Store (CDS). (Accessed on < 06-03-2022 >), <https://doi.org/10.24381/cds.adbb2d47>.

437

438 Kato, S., Rose, F. G., Rutan, D. A., Thorsen, T. E., Loeb, N. G., Doelling, D. R., Huang, X., Smith, W. L., Su, W., and Ham, S.-  
439 H.: Surface irradiances of Edition 4.0 Clouds and the Earth's Radiant Energy System (CERES) Energy Balanced and Filled (EBAF)  
440 data product, *J. Climate*, 31, 4501–4527, <https://doi.org/10.1175/JCLI-D-17-0523.1>, 2018.

441

442 Kleidon, A., and M. Renner, 2017: An explanation for the different climate sensitivities of land and ocean surfaces based on the  
443 diurnal cycle. *Earth Syst. Dynam.*, 8, 849–864. <https://doi.org/10.5194/esd-8-849-2017>

444

445 Lee, S., T. Gong, S. B. Feldstein, J. A. Screen, and I. Simmonds, 2017: Revisiting the Cause of the 1989–2009 Arctic Surface  
446 Warming Using the Surface Energy Budget: Downward Infrared Radiation Dominates the Surface Fluxes. *Geophysical Research*  
447 *Letters*, 44, 10,654–610,661. <https://doi.org/10.1002/2017GL075375>.

448

449 Loeb, N. G., Doelling, D. R., Wang, H., Su, W., Nguyen, C., Corbett, J. G., Liang, L., Mitrescu, C., Rose, F. G., and Kato, S.:  
450 Clouds and the Earth's Radiant Energy System (CERES) Energy Balanced and Filled (EBAF) Top-of-Atmosphere (TOA) Edition-  
451 4.0 data product, *J. Climate*, 31, 895–918, <https://doi.org/10.1175/JCLI-D-17-0208.1>, 2018.

452

453 Esmael Malek, 1997. Evaluation of effective atmospheric emissivity and parameterization of cloud at local scale. *Atmospheric*  
454 *Research*, 45 (1), 41–54. [https://doi.org/10.1016/S0169-8095\(97\)00020-3](https://doi.org/10.1016/S0169-8095(97)00020-3).

455

456 Monteith, J.L. and Unsworth, M.H. (2008) *Principles of Environmental Physics*. 3rd Edition, Academic Press, New York, 418.

457

458 NASA/LARC/SD/ASDC. (2017). CERES and GEO-Enhanced TOA, Within-Atmosphere and Surface Fluxes, Clouds and  
459 Aerosols Monthly Terra-Aqua Edition4A [Data set]. NASA Langley Atmospheric Science Data Center DAAC. (Accessed on <  
460 09-03-2022 >), [https://doi.org/10.5067/TERRA+AQUA/CERES/SYN1DEGMONTH\\_L3.004A](https://doi.org/10.5067/TERRA+AQUA/CERES/SYN1DEGMONTH_L3.004A).

461

462 [Panwar, A., and A. Kleidon, 2022: Evaluating the Response of Diurnal Variations in Surface and Air Temperature to Evaporative](#)  
463 [Conditions across Vegetation Types in FLUXNET and ERA5. \*J. Climate\*, 35, 6301–6328, https://doi.org/10.1175/JCLI-D-21-](#)  
464 [0345.1.](#)

465

466 Park, H.-S., S. Lee, S.-W. Son, S. B. Feldstein, and Y. Kosaka, 2015: The impact of poleward moisture and sensible heat flux on  
467 Arctic winter sea ice variability. *J. Climate*, 28, 5030–5040, <https://doi.org/10.1175/JCLI-D-15-0074.1>

468

469 Pastorello, G., and Coauthors, 2020: The FLUXNET2015 dataset and the ONEFlux processing pipeline for eddy covariance data.  
470 *Scientific Data*, 7, 225. <https://doi.org/10.1038/s41597-020-0534-3>

471

472 [Prata, A.J. \(1996\). A new long-wave formula for estimating downward clear-sky radiation at the surface. \*Q.J.R. Meteorol. Soc.\*,](#)  
473 [122: 1127–1151. https://doi.org/10.1002/qj.49712253306](#)

474

475 [Previdi, M. \(2010\). Radiative feedbacks on global precipitation. \*Environmental Research Letters\*, 5, 025211.](#)  
476 <https://doi.org/10.1088/1748-9326/5/2/025211>

477

478 Sridhar V, Ronald L Elliott, 2022: On the development of a simple downwelling longwave radiation scheme, *Agricultural and*  
479 *Forest Meteorology*, 112, 3–4, 237–243, [https://doi.org/10.1016/S0168-1923\(02\)00129-6](https://doi.org/10.1016/S0168-1923(02)00129-6).

480

481 Satterlund, D. R., 1979: An improved equation for estimating long-wave radiation from the atmosphere. *Water Resources Research*,  
482 15, 1649–1650. <https://doi.org/10.1029/WR015i006p01649>

483

484 [Shakespeare C. J. and M. Roderick. \(2022\). Diagnosing Instantaneous Forcing and Feedbacks of Downwelling Longwave](#)  
485 [Radiation at the Surface: A Simple Methodology and Its Application to CMIP5 Models. \*Journal of Climate\*.](#)

486

设置了格式: 字体颜色: 黑色

域代码已更改

域代码已更改

域代码已更改

域代码已更改

域代码已更改

域代码已更改

域代码已更改

域代码已更改

域代码已更改

域代码已更改

域代码已更改

487 Su, J., A. Duan, and H. Xu, 2017: Quantitative analysis of surface warming amplification over the Tibetan Plateau after the late  
488 1990s using surface energy balance equation. *Atmospheric Science Letters*, 18, 112-117. <https://doi.org/10.1002/asl.732>

489  
490 Tian, Y., Zhang, Y., Zhong, D., Zhang, M., Li, T., Xie, D., & Wang, G. (2022). Atmospheric Energy Sources for Winter Sea Ice  
491 Variability over the North Barents–Kara Seas, *Journal of Climate*, 35(16), 5379-5398. <https://doi.org/10.1175/JCLI-D-21-0652.1>

492  
493 Trenberth, K. E., Fasullo, J. T., & Kiehl, J. (2009). Earth's Global Energy Budget, *Bulletin of the American Meteorological*  
494 *Society*, 90(3), 311-324. <https://doi.org/10.1175/2008BAMS2634.1>

495  
496 Monteith, J.L., and Unsworth, M.H. 2008. *Principles of Environmental Physics*. Third Ed. AP, Amsterdam.  
497 <http://store.elsevier.com/Principles-of-Environmental-Physics/John-Monteith/isbn-9780080924793/>.

498  
499 UNCOD Secretariat (1977) *Desertification: Its causes and consequences*, Pergamon Press, 448 p.

500  
501 Vargas Zeppetello, L. R., Donohoe, A., & Battisti, D. S. (2019). Does surface temperature respond to or determine downwelling  
502 longwave radiation? *Geophysical Research Letters*, 46, 2781–2789. <https://doi.org/10.1029/2019GL082220>

503  
504 Viúdez-Mora, A., Costa-Surós, M., Calbó, J., and González, J. A. (2015). Modeling atmospheric longwave radiation at the surface  
505 during overcast skies: The role of cloud base height. *J. Geophys. Res. Atmos.*, 120, 199–214.  
506 <https://doi.org/10.1002/2014JD022310>

507  
508 Wang, K., and S. Liang, 2009: Global atmospheric downward longwave radiation over land surface under all-sky conditions from  
509 1973 to 2008. *Journal of Geophysical Research: Atmospheres*, 114. <https://doi.org/10.1029/2009JD011800>

510  
511 Wei, Y., and Coauthors, 2021: Trends and Variability of Atmospheric Downward Longwave Radiation Over China From 1958 to  
512 2015. *Earth and Space Science*, 8, e2020EA001370. <https://doi.org/10.1029/2020EA001370>

513  
514 Wild, M., Folini, D., Hakuba, M.Z. et al. The energy balance over land and oceans: an assessment based on direct observations and  
515 CMIP5 climate models. *Clim Dyn* 44, 3393–3429 (2015). <https://doi.org/10.1007/s00382-014-2430-z>

516  
517 Wild, M., Ohmura, A., Schär, C., Müller, G., Folini, D., Schwarz, M., Hakuba, M. Z., and Sanchez-Lorenzo, A.: The Global Energy  
518 Balance Archive (GEBA) version 2017: a database for worldwide measured surface energy fluxes, *Earth Syst. Sci. Data*, 9, 601–  
519 613. <https://doi.org/10.5194/essd-9-601-2017>, 2017.

520  
521 Xie, P., Chen, M., Yang, S., Yatagai, A., Hayasaka, T., Fukushima, Y., & Liu, C. (2007). A Gauge-Based Analysis of Daily  
522 Precipitation over East Asia, *Journal of Hydrometeorology*, 8(3), 607-626. <https://doi.org/10.1175/JHM583.1>.

523  
524 Zampieri, M., F. D'Andrea, R. Vautard, P. Ciais, N. de Noblet-Ducoudré, and P. Yiou, 2009: Hot European Summers and the Role  
525 of Soil Moisture in the Propagation of Mediterranean Drought. *Journal of Climate*, 22, 4747-4758.  
526 <https://doi.org/10.1175/2009JCLI2568.1>

527  
528 Zhou and Savijärvi, 2014. The effect of aerosols on long wave radiation and global warming. *Atmospheric Research*, 135–136:  
529 102-111 <https://doi.org/10.1016/j.atmosres.2013.08.009>

530

域代码已更改

域代码已更改

域代码已更改

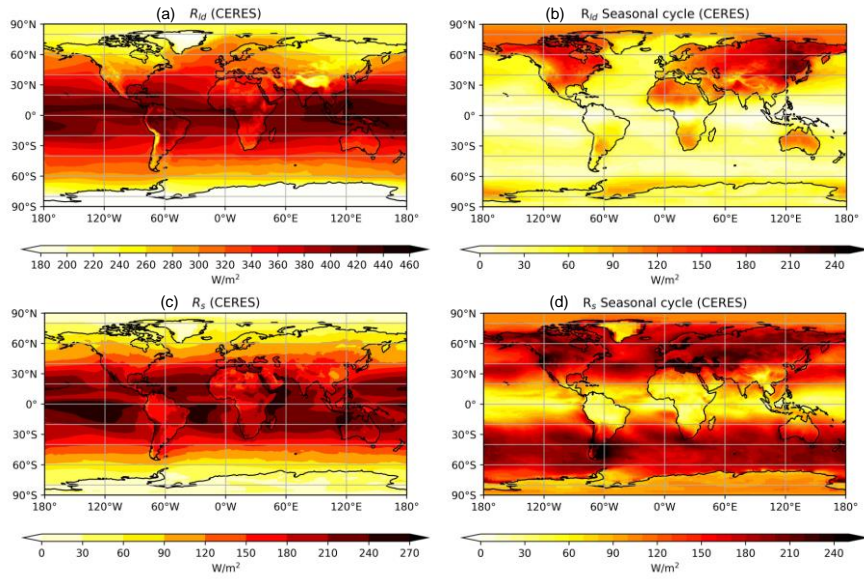
域代码已更改

域代码已更改

域代码已更改

域代码已更改

531 **Figures**



532

533

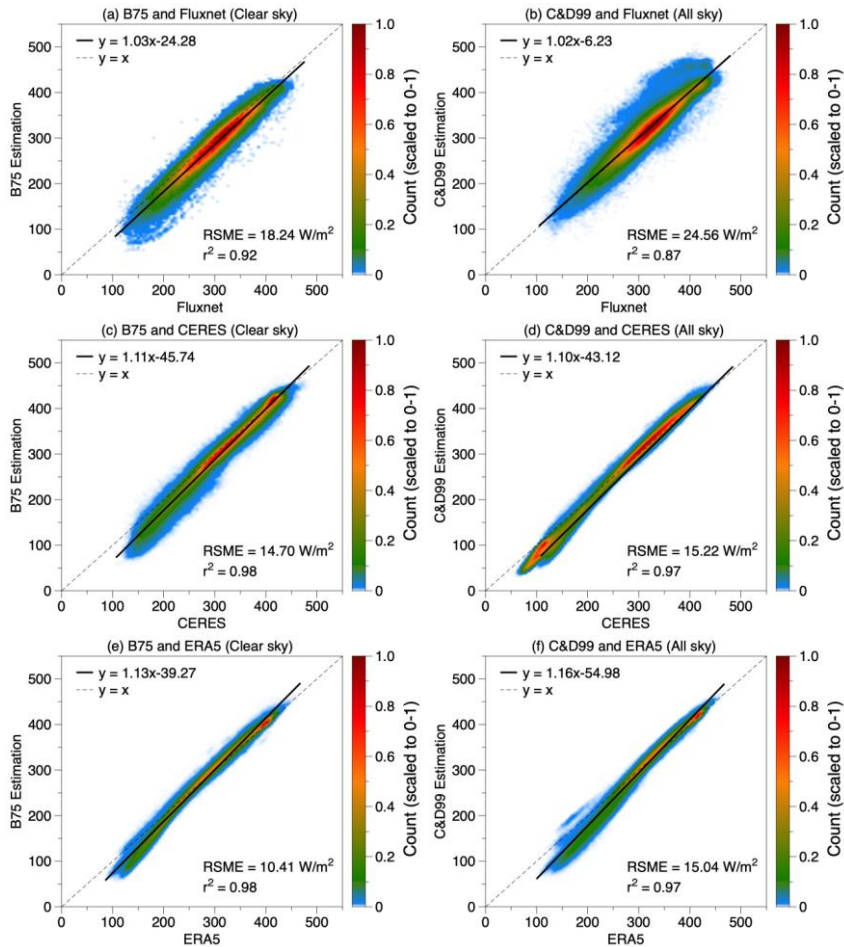
534

535

536

537

**Figure 1.** Spatial distribution of (a, c) (a, c) the climatological mean and (b, d) (b, d) the seasonal amplitude of downward longwave radiation and absorbed solar radiation at the surface respectively from the NASA-CERES dataset. The seasonal amplitude is calculated as the difference between the maximum and minimum monthly data.

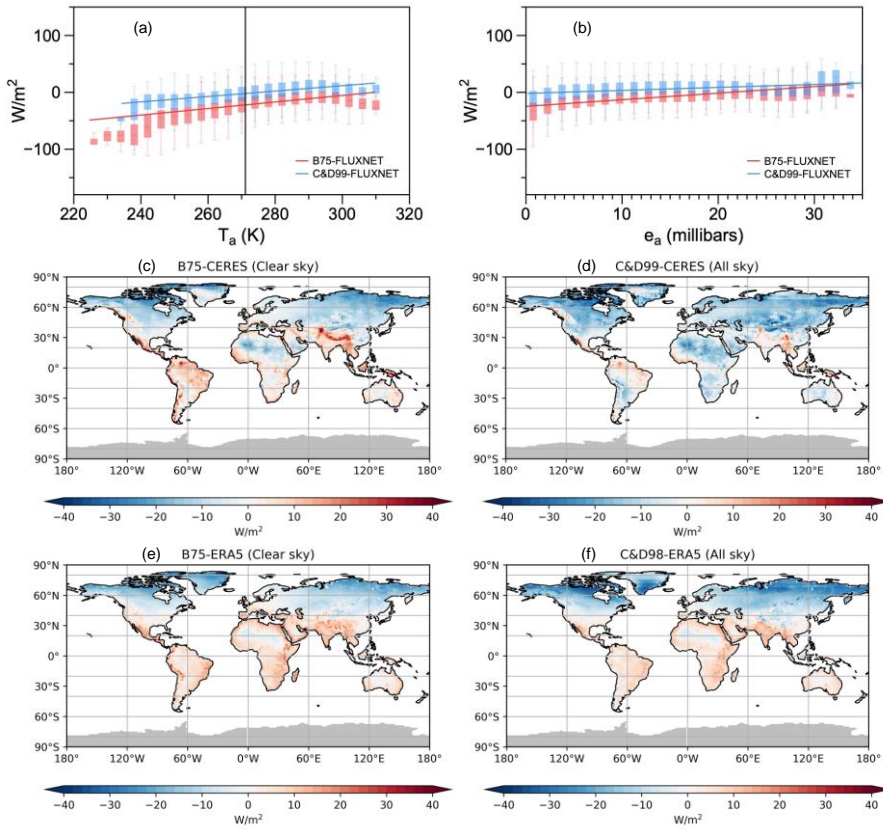


538  
 539 Figure 2. Comparison of  $R_{ld}$  estimated by Brutsaert (1975) (a, c, e) for clear-sky conditions and by  
 540 Crawford and Duchon (1999) (b, d, f) for all-sky conditions using (a, b) FLUXNET hourly data of 189  
 541 sites, (c, d) NASA-CERES monthly data of  $1^\circ \times 1^\circ$  from 2001 to 2018 and (e, f) ERA5 monthly data of  
 542 resolution of  $1^\circ \times 1^\circ$  from 1979 to 2021. Colors indicate the density of the data points and is scaled to values  
 543 between 0 - 1.

544 Comparison of  $R_{ld}$  estimated (a, c, e) by Brutsaert (1975) for clear sky conditions and (b, d, f) by Crawford  
 545 and Duchon (1999) for all sky conditions using FLUXNET hourly data of 189 sites (a, b), NASA CERES

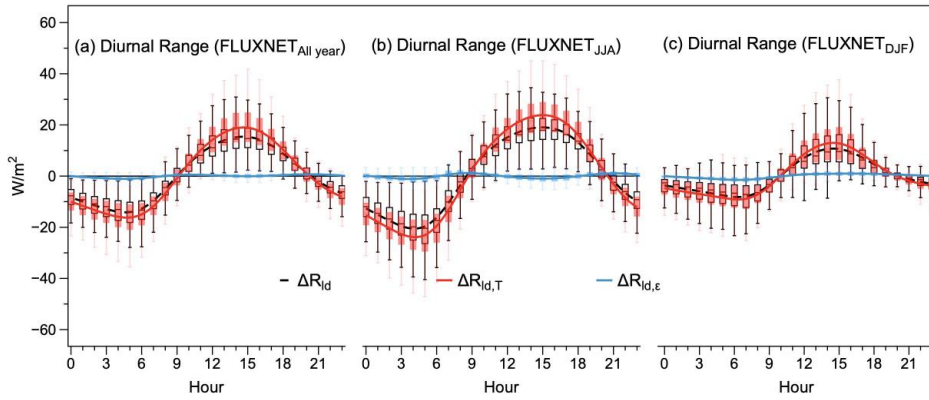
- 设置了格式: 字体: 四号
- 设置了格式: 字体: (默认) Times New Roman, 11 磅
- 设置了格式: 字体: (默认) Times New Roman, 11 磅
- 设置了格式: 字体: (默认) Times New Roman, 11 磅
- 设置了格式: 字体: (默认) Times New Roman, 11 磅
- 设置了格式: 字体: (默认) Times New Roman, 11 磅
- 设置了格式: 字体: (默认) Times New Roman, 11 磅

546 monthly data of  $1^\circ \times 1^\circ$  from 2001 to 2018 (c, d) and ERA5 half monthly data of resolution of  $1^\circ \times 1^\circ$  from  
 547 1979 to 2021 (e, f). Colors indicate the density of the data points and is scaled to values between 0–1.

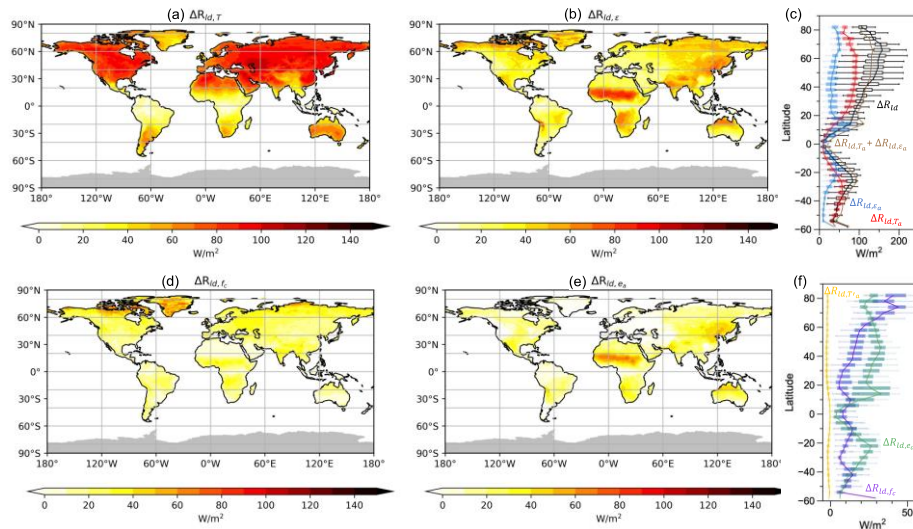


548  
 549 **Figure 3.** Biases in the estimates for multi-year mean  $R_{id}$  for FLUXNET data of 189 sites against (a) air  
 550 temperature (a) and (b) water vapor pressure (b). Distribution of biases in the estimates for multi-year mean  
 551  $R_{id}$  for (c, d) NASA-CERES data from 2001 to 2018 and (e, f) ERA reanalysis from 1979 to 2021 for (c, e)  
 552 clear-sky and (d, f) all-sky conditions over land. Grey shading indicates missing values.  
 553

带格式的: 题注, 左



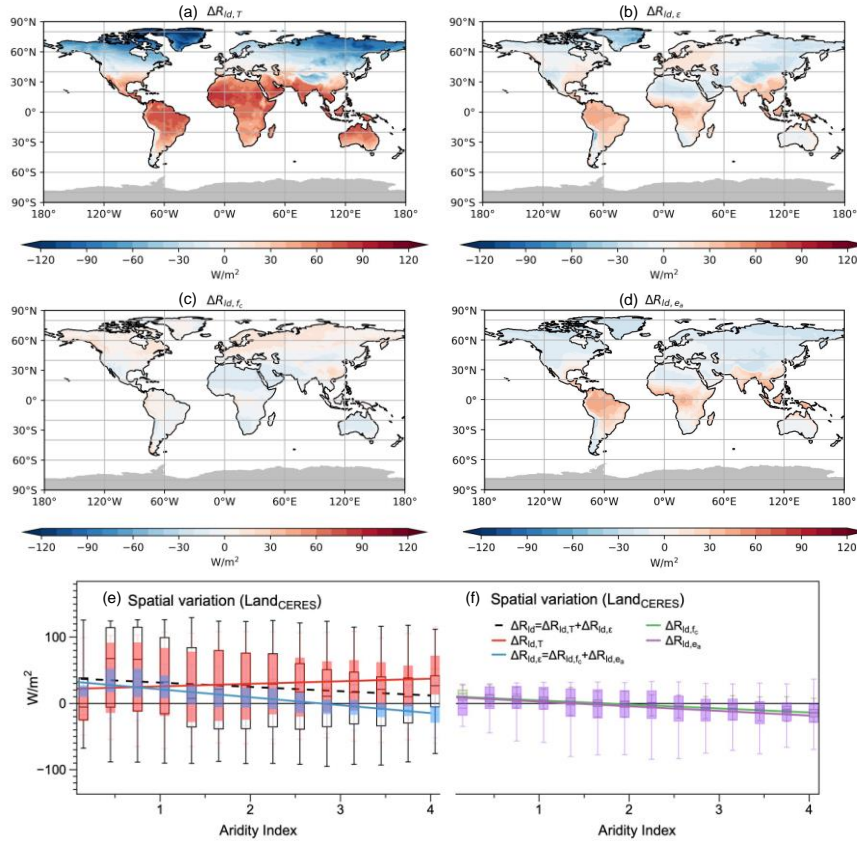
554  
 555 **Figure 4.** The multi-year average diurnal variations in  $R_{ld}$  (black dashed line) and its decomposition into  
 556 contributions by changes in emissivity (blue,  $\Delta R_{ld,\epsilon}$ ) and lower-level atmospheric heat storage (red,  $\Delta R_{ld,T}$ )  
 557 in the FLUXNET dataset aggregated over 189 sites for (a) the whole year, (b) June-August, and  
 558 (c) December-February. The box shows the variation among the 189 sites. The upper and lower  
 559 whiskers indicate 95<sup>th</sup> and 5<sup>th</sup> percentiles, upper boundary, median line, and lower boundary of the  
 560 box indicate the 75<sup>th</sup>, 50<sup>th</sup>, and 25<sup>th</sup> quantiles, respectively. For each site and each day, the daily mean value  
 561 is removed, with the deviations shown. Regression lines are based on site-mean or grid-mean value using  
 562 LOESS regression.  
 563



564  
 565 **Figure 5.** Decompositions of the mean seasonal variation ( $\Delta$ , difference between the maximum and  
 566 minimum monthly data at each grid) of  $R_{ld}$  in the NASA-CERES dataset into contributions by (a) lower-  
 567 level atmospheric heat storage ( $\Delta R_{ld,T}$ ) and (b) emissivity ( $\Delta R_{ld,\epsilon}$ ) and (c) their latitudinal



568 variations. (e) Decomposed of  $\Delta R_{ld,\varepsilon}$  into contributions by variations in (d) cloud cover ( $\Delta R_{ld,fc}$ ) (e) and  
 569 (e) humidity ( $\Delta R_{ld,ea}$ ), (f) their latitudinal variations. (f) In Figs. a, b, d, e, grey shading indicates  
 570 missing values. In Figs. c and f, the box shows the variation among the land grids at the same latitude, while  
 571 the solid line is their mean. The upper and lower whisker indicate 95<sup>th</sup> and 5<sup>th</sup> percentiles, upper boundary,  
 572 median line, and lower boundary of the box indicate the 75<sup>th</sup>, 50<sup>th</sup>, 25<sup>th</sup> quantiles, respectively.  
 573



574  
 575 **Figure 6.** Decompositions of the multiyear-mean spatial variation of  $R_{ld}$  (deviations of the multiyear-mean  
 576 value for each grid from the land-mean value) in the NASA-CERES dataset into contributions by (a) lower-  
 577 level atmospheric heat storage ( $\Delta R_{ld,\tau}$ ) (a) and (b) emissivity ( $\Delta R_{ld,\varepsilon}$ ). (b) Decomposition of  $\Delta R_{ld,\varepsilon}$   
 578 into contributions by (c) variations in cloud cover ( $\Delta R_{ld,fc}$ ) (c) and (d) humidity ( $\Delta R_{ld,ea}$ ) (d). In Figs.  
 579 a-d, grey shading indicates missing values. In Figs. e and f, the box shows the variation among the land  
 580 grids with the same aridity. The upper and lower whisker indicate 95<sup>th</sup> and 5<sup>th</sup> percentiles, upper boundary,  
 581 median line, and lower boundary of the box indicate the 75<sup>th</sup>, 50<sup>th</sup>, 25<sup>th</sup> quantiles, respectively.  
 582  
 583  
 584  
 585

586 Plain Language:

587  
588 Downward longwave radiation ( $R_{ld}$ ) plays an important role in surface energy balance and is critical for  
589 global warming. However, its spatiotemporal climatological variation on a global scale has not been  
590 explained well with a solid physical basis. To fill this gap, we here use a semi-empirical equation derived  
591 by Brutsaert (1975, "B75") and its extension by Crawford and Duchon (1999, "C&D99") to identify the  
592 leading terms responsible for the diurnal range, seasonal cycle, and geographical variations in  $R_{ld}$ . We show  
593 that B75 and C&D99 work very well when evaluated against global observations from satellites and  
594 FLUXNET sites. We then used these physics-based equations to show that diurnal and seasonal variations  
595 in  $R_{ld}$  are predominantly controlled by changes in atmospheric heat storage. When moving from humid to  
596 arid regions, while the contribution of atmospheric heat storage increases, the ones from clouds decreases,  
597 which together explains the relatively small decrease in  $R_{ld}$  with aridity. Our work provides a clue to better  
598 understand aspects of climate variability, extreme events, and global warming, by linking these to the  
599 mechanistic contributions by downwelling longwave radiation.

600